

2017

Design and Investigation of de Vries Liquid Crystals Based on 5-Phenyl-Pyrimidine and (R,R)-2,3-Epoxyhexoxy backbone.

S.P. Sreenilayam^{*}

Trinity College Dublin, Ireland

D. Rodriguez-Lojo

Queens University, Belfast

V. P. Panov

Trinity College Dublin, Ireland

See next page for additional authors

Follow this and additional works at: <https://arrow.tudublin.ie/engscheleart2>

 Part of the [Electrical and Electronics Commons](#)

Recommended Citation

Sreenilayam, S.P., Rodriguez-Lojo, D. & Panov, V.P. (2017). Design and Investigation of de Vries Liquid Crystals Based on 5-Phenyl-Pyrimidine and (R,R)-2,3-Epoxyhexoxy backbone. *Physical Review*, vol. 96, no. 4. doi:10.1103/PhysRevE.96.042701

This Article is brought to you for free and open access by the School of Electrical and Electronic Engineering at ARROW@TU Dublin. It has been accepted for inclusion in Articles by an authorized administrator of ARROW@TU Dublin. For more information, please contact arrow.admin@tudublin.ie, aisling.coyne@tudublin.ie.



This work is licensed under a [Creative Commons Attribution-NonCommercial-Share Alike 4.0 License](#)

Authors

S.P. Sreenilayam", D. Rodriguez-Lojo, V. P. Panov, V. Swaminathan, J. K. Vij, Yuri Panarin, E. Gorecka, A. Panov, and P.J. Stevenson

This is the accepted manuscript made available via CHORUS. The article has been published as:

Design and investigation of de Vries liquid crystals based on 5-phenyl-pyrimidine and (R,R)-2,3-epoxyhexoxy backbone

S. P. Sreenilayam, D. Rodriguez-Lojo, V. P. Panov, V. Swaminathan, J. K. Vij, Yu. P. Panarin, E. Gorecka, A. Panov, and P. J. Stevenson

Phys. Rev. E **96**, 042701 — Published 3 October 2017

DOI: [10.1103/PhysRevE.96.042701](https://doi.org/10.1103/PhysRevE.96.042701)

The design and investigation of de Vries liquid crystals based on 5-phenyl-pyrimidine and (R,R)-2,3-epoxyhexoxy backbone

S. P. Sreenilayam,¹ D. Rodriguez-Lojo,² V. P. Panov,¹ V. Swaminathan,¹ J. K. Vij,^{1*} Y. P. Panarin^{1,3} E. Gorecka,⁴ A. Panov,² P. J. Stevenson²

¹Department of Electronic and Electrical Engineering, Trinity College Dublin, The University of Dublin, Dublin 2, Ireland

²School of Chemistry and Chemical Engineering, Queens University, Belfast, BT7 1NN, United Kingdom

³School of Electrical and Electronic Engineering, Dublin Institute of Technology, Dublin 8, Ireland

⁴Department of Chemistry, Warsaw University, Al. Zwirki i Wigury 101, 02089 Warsaw, Poland

Calamitic liquid crystals (LCs) based on 5-phenyl-pyrimidine derivatives have been designed, synthesized and characterized. The 5-phenyl pyrimidine core was functionalized with chiral (R,R)-2,3-epoxyhexoxy chain on one side and either siloxane or perfluoro terminated chains on the opposite side. The one involving perfluorinated chain shows SmA* phase over a wide temperature range of 82 °C, whereas the siloxane analogue exhibits both SmA* and SmC* phases over broad range of temperatures and a weak first order SmA* - SmC* transition is observed. For the siloxane analogue, the reduction factor for the layer shrinkage R (relative to its thickness at the SmA* - SmC* transition temperature, T_{AC}) is ~ 0.373 and layer shrinkage is 1.7% both at a temperature of 13 °C below the T_{AC} . This compound is considered to be having “de Vries smectic” characteristics with the de Vries coefficient, $C_{deVries}$ of ~ 0.86 on the scale of zero (the maximum layer shrinkage) to 1 (zero layer shrinkage). A three-parameter mean-field model is introduced for the orientational distribution function (ODF) to reproduce the electro-optic properties. This model explains the experimental results and leads to the ODF which exhibits a cross-over from the sugar-loaf to diffuse-cone ODF some 3 °C below T_{AC} .

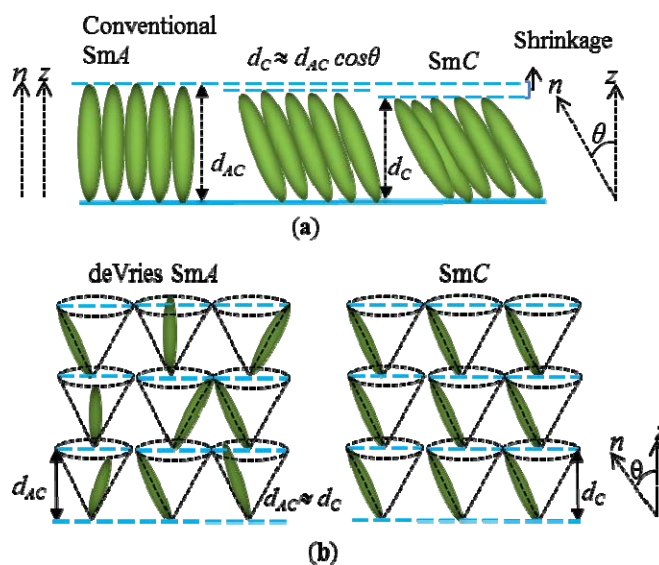
Email: jvij@tcd.ie

34 I. INTRODUCTION

35 Chiral smectic liquid crystals (LCs) having mesophases close to the room temperature
 36 are extremely useful for the next generation of displays and electro-optical devices. The
 37 devices based on ferroelectric smectics with extremely fast switching time (μs) compared to
 38 the currently used slowly switching nematics (ms) are very promising [1]. However to obtain
 39 the defect free alignment in an LC cell over a broad range of temperatures, a pre-requisite of
 40 zero or a small layer shrinkage for practical applications is required and the achievement of
 41 which is still an open challenge. In principle, one is able to align the material very well in the
 42 nematic or smectic A phases. However on a phase transition from $\text{Sm}A$ to $\text{Sm}C$, a tilt emerges
 43 whereby the molecular long axis \mathbf{n} tilts relative to the layer normal \mathbf{z} by an angle, θ , that varies
 44 with temperature (Fig. 1a). Consequently, the layer spacing (d_C) in the $\text{Sm}C$ phase decreases
 45 by a factor of $\cos\theta$ provided liquid crystalline molecules are close enough to being considered
 46 as rigid rods. The layer shrinkage arising from the tilt together with surface anchoring of
 47 molecules leads to chevron structure/s formed in the cell. These structures with opposite fold
 48 directions create zigzag defects at the interface in between the two oppositely folded
 49 cheverons. The emergence of these defects are impediments to a successful
 50 commercialization of devices based on ferroelectric LCs [2-4]. The solution is therefore
 51 focussed on to developing chiral LCs with a minimal or zero layer-shrinkage at the $\text{Sm}A^*$ -
 52 $\text{Sm}C^*$ transition temperature and within the temperature range of $\text{Sm}C^*$ [4]. It is normally
 53 the case that where the layer shrinkage is much lower than the scaling factor, $\cos\theta$, then the
 54 smectic phases of such compounds are known as ‘de Vries smectics’ (Fig. 1b).

55 A dozen or so compounds have been identified to have de Vries characteristics to the
 56 varying degrees of perfection. According to the semi-qualitative studies carried out so far, the
 57 calamitic LCs that combine low orientational order parameter but large lamellar orderings
 58 are likely to exhibit better de Vries type characteristics [5-9]. Most of the de Vries smectics
 59 contain trisiloxane/carbosilane backbones and perfluorinated side chains on either ends of the
 60 core; these terminations strongly promote lamellar orderings [10]. In this case, the alkane
 61 chains were replaced by an epoxy group (a precursor in the synthesis of the difluoro
 62 material). In order to obtain a large P_S in the $\text{Sm}C^*$ phase, it is pertinent to prepare highly
 63 enantiomeric enriched chiral molecules to avoid the cancelation effects of the oppositely

handed enantiomers. In the literature, excellent protocols are given for preparing epoxides from allylic alcohols with large enantiomeric excesses [11]. However to our knowledge, materials with enantiomeric enriched 5-phenyl pyrimidine epoxides have not yet been reported to have de Vries like behavior [12] before. The epoxide group may induce large electrical polarization. A use of 5-phenyl pyrimidine though as an aromatic core is extensively used in the synthesis of compounds that exhibit de Vries-like characteristics in chiral and non-chiral mesogens [13-15]. With this concept in mind, two new chiral materials containing epoxides in their structures have been designed, synthesized and investigated.



72

FIG. 1 Schematic representation of the molecular arrangements in the SmA and SmC mesophases as per (a) conventional rigid-rod model and, (b) de Vries diffuse cone model [16]. z is the layer normal, n is the molecular long axis orientation, θ is the angle between n and z , d_C and d_A are the layer spacing in SmC and SmA, respectively.

In this article, we report synthesis and properties of the two 5-phenyl pyrimidine derivatives that contain the chiral (*R,R*)-2,3-epoxyhexoxy chain in conjunction with trisiloxane (adpc042) or perfluorinated (DR257) terminal chains (see appendix for the synthetic procedure). Both moieties are therefore structurally related to each other, both use the same aromatic core and the epoxide chiral chain. In the DR257, siloxane group is replaced with perfluorinated butane as aliphatic linkage of six carbons with the aromatic core. A modification of the chain ending could have a significant effect on the properties and with the objective of finding its effect on the electro-optic properties, we decided to explore this further to establish a well-desired structure-property relationship. The mesophases formed by these compounds were characterized by differential scanning calorimetry (DSC), polarized

optical microscopy (POM), x-ray diffraction (XRD), electro-optics and dielectric spectroscopy. Characterization of the LCs shows that the perfluorinated epoxide DR257 exhibits a stable SmA* phase over a broad range of temperatures whereas the siloxane terminated analogue adpc042 exhibits both SmA* and SmC* phases. In this trisiloxane compound we achieve a layer shrinkage of 1.7 %, at a temperature of -13 °C below the SmA* - SmC* transition temperature. Since adpc042 LC exhibits both SmA* and SmC* phases, properties of this compound are detailed below.

II. EXPERIMENT

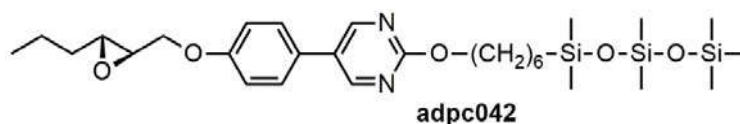
The phase sequence and the transition temperatures were found by DSC thermograms (Perkin-Elmer DSC-7 calorimeter). The experiment was carried out under cooling at a rate of 10 °C min⁻¹. The electro-optical studies of the two LCs were conducted using planar-aligned cells with parallel rubbed polyimide alignment layer KSRP-XX/D611P6NSS05. These cells were purchased from EHC, Japan. LC cells were studied by POM and electro-optics . Olympus BX 52, equipped with a rotating table was used. The hot-stage was fixed on to the rotating table. The hot stage was connected to a temperature controller, Eurotherm 2604. XRD measurements were carried out on Bruker D8 diffractometer using Cu-K_α source with a wavelength 0.154 nm. Dielectric spectroscopic studies were performed using an Alpha High Resolution Dielectric Analyser (Novocontrol GmbH, Germany) in the frequency range 1 Hz - 10 MHz. Indium Tin Oxide (ITO) coated glass substrates were used to make cells for studies of the real and imaginary parts of the dielectric permittivity. Substrates were coated with RN 1175 polymer (Nissan Chemicals, Japan) for obtaining the planar alignment. The cell thickness (*d*) was controlled by Mylar spacers. UV-VIS spectrometer (Avaspec-2048) was used to measure *d* through interference fringes. The ITO sheet resistance of the substrates (20 Ω/□) is low enough to shift the peak frequency for the resistance of the ITO in series with the cell, beyond the experimental window of measurements. The dielectric spectra were analysed using Novocontrol WINDETA program.

III. RESULTS AND DISCUSSIONS

A. Differential Scanning Calorimetry and Polarizing Optical Microscopic Studies

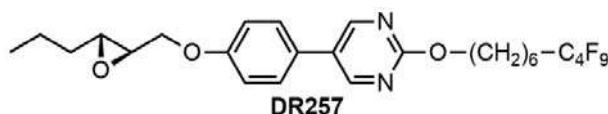
The molecular structure and the transition temperatures of siloxane pyrimidine adpc042 and the fluorinated pyrimidine DR257 are given in Figs. 2 (a) and (b) (synthetic

procedures given in the appendix). Result of a DSC thermogram of DR257 is given in Fig. 2c. Here two transitions with the enthalpies, ΔH of $\sim 17.2 \text{ Jg}^{-1}$ and $\sim 30.4 \text{ Jg}^{-1}$ at temperatures of $\sim 143^\circ\text{C}$ and $\sim 56^\circ\text{C}$ are recorded. To identify the mesophases, textures of a $9 \mu\text{m}$ planar cell filled with DR257 are recorded with POM. Images corresponding to the two mesophases are shown in the inset of Fig. 2c. On cooling from the isotropic temperature, the mesophase grows from the typical ‘batonnet’ structures to the focal conic texture. Both focal conic and dark homeotropic textures obtained by POM are the characteristics of SmA^* phase [17]. Textures confirm that the phase transition from SmA^* to a crystalline state is at a temperature of 56°C .



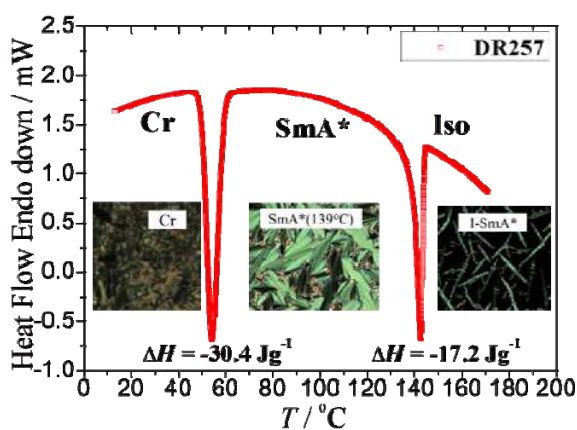
Cr -5°C SmC^* 58°C SmA^* 82°C Iso

(a)

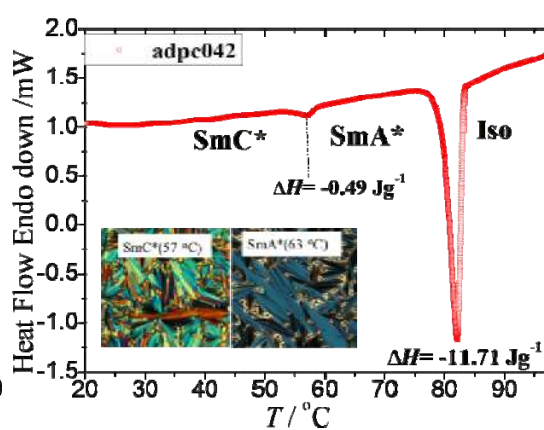


Cr 60°C SmA^* 152°C Iso

(b)



(c)



(d)

FIG. 2 Molecular structures and the DSC thermograms of adpc042 [(a) and (d)] and DR257 [(b) and (c)] are given. The phase transition temperatures are obtained under the cooling cycle with a quasi-equilibrium condition at the rate of $\sim 1^\circ\text{C min}^{-1}$ using POM. The cooling curves of the DSC thermograms are obtained at the rate of $10^\circ\text{C min}^{-1}$. Iso= isotropic phase, Cr= crystalline state. Insets in these two figures are the POM images of the mesophases seen under the crossed polarizers. Textures are recorded for a $9 \mu\text{m}$ planar-aligned cells in the cooling run.

A representative the DSC plot of adpc042 LC under cooling exhibits two peaks (Fig. 2d). Both DR257 and adpc042 show the first order Iso-SmA* transition with ΔH of $\sim 11.71 \text{ Jg}^{-1}$ and 17.2 Jg^{-1} at a temperature of $\sim 82^\circ\text{C}$ and $\sim 145^\circ\text{C}$. This is confirmed by POM where the focal conic fan shaped texture from a $9 \mu\text{m}$ planar-aligned cell (Fig. 2d inset) is recorded. On lowering the temperature, the sample undergoes a weakly first order SmA* - SmC* transition with ΔH of $\sim 0.49 \text{ Jg}^{-1}$ ($0.069 \text{ kcal mol}^{-1}$) at 58°C [12, 18]. For a conventional SmA* - SmC* transition where the tilt angle stays at almost zero value in the SmA* phase down to the transition temperature T_{AC} , the DSC thermogram exhibits a second order transition with a step in the baseline without a peak for the enthalpy of transition [19]. The SmC* phase of adpc042 is distinguishable from SmA* by POM where a fan shaped texture from a planar cell is altered to a broken fan shaped one (inset Fig. 2d). The dark homeotropic texture is changed to Schlieren texture on transition from SmA* to SmC*. The entire replacement of trisiloxane in adpc042 by tetra fluorocarbon chain in DR257, radically alters the mesomorphic behaviour, the temperature range of SmA* is increased from 23°C to 89°C , whereas SmC* disappears. An increased temperature range of the SmA* phase in DR257 could be due to a large dipole moment associated with the fluorinated tail [20]. The siloxane groups in adpc042 enhance the thermal stability of the compound as well as lower the phase transition temperatures. These features may be of great importance from a point of view of the molecular design and applications.

The POM images of a planar-aligned cell of thickness $9 \mu\text{m}$ filled with adpc042 recorded at 63°C ($\sim 19^\circ\text{C}$ below the Iso-SmA* transition temperature and 5°C above the T_{AC}), are given in Fig. 3. The rubbing direction R_d is fixed at an angle, $\alpha = \sim 15^\circ$ to the polarizer \mathbf{P} .

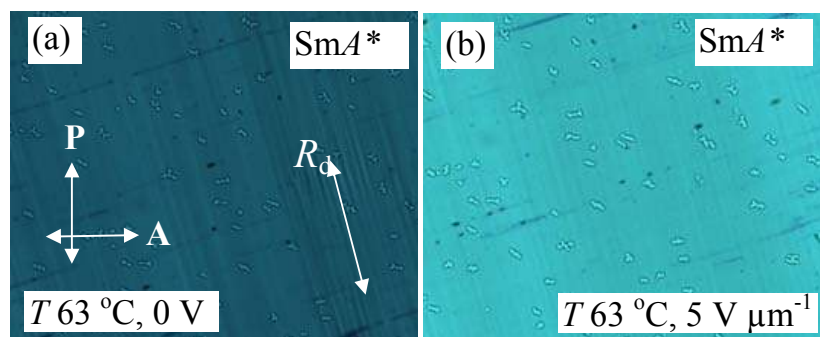


FIG. 3 POM images of SmA* phase at a temperature of 63°C in a $9 \mu\text{m}$ planar-aligned cell filled with adpc042 LC: (a) 0 V and (b) $5 \text{ V } \mu\text{m}^{-1}$ (square wave AC electric field of 110 Hz).

The electric field treatment of the LC cell gives rise to a uniform mono-domain texture (Fig. 3). An application of the external electric field across a cell in well-aligned SmA* phase produces a change in the color of the texture (compare Figs. 3a and 3b), due to an increase in the birefringence Δn with the field, a characteristic of the de Vries behavior. In this phase, the molecules are tilted but are azimuthally disordered. The electric field produces a bias in the azimuthal distribution and the molecules tilt in a particular direction determined by the polarity of the field. The resulting SmA* is reduced to the same symmetry as SmC* phase through azimuthal ordering of the already tilted liquid crystalline molecules.

B. X-ray diffraction(XRD)

Figure 4(a) shows the temperature dependence of the smectic layer spacing determined by the XRD experiment. On cooling the sample below the isotropic phase, the layer spacing in SmA* phase initially increases linearly with decreasing temperature. On approaching the SmA*- SmC* transition temperature, the thickness reverses its trend within SmA* from an increase to a decrease due to an emergence of the molecular tilt even in the SmA* phase. On further cooling of the sample cell, the layer thickness in the SmC* phase continues to decrease much more slowly than expected from a conventional smectic, in which the layer thickness scales as, $\cos \theta$. Figure 4b shows the simulated molecular structures of the compound adpc042 using Hyperchem Program. The simulated length l , of the molecule is ~ 31 Å. A possible molecular arrangement in layers is shown in Fig. 4b such that the total length of a pair of molecules is larger than the smectic layer thickness.

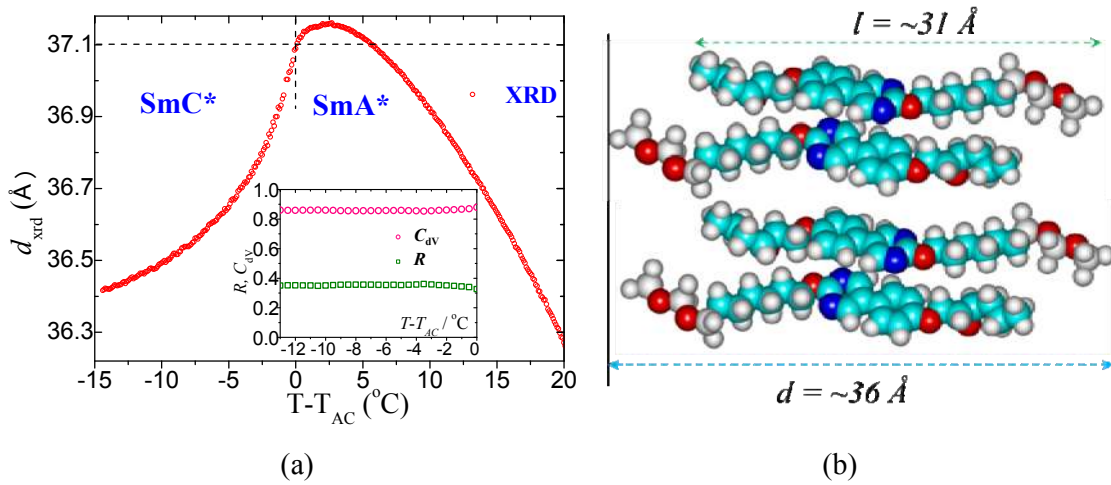


FIG. 4 (a) Temperature dependence of the smectic layer spacing determined by XRD (\blacktriangle) relative to the layer thickness at the SmA* to SmC* transition temperature. The inset shows plots of the de Vries coefficient C_{deVries} (\square) and the reduction factor R (\square) vs. the

reduced temperature ($T-T_{AC}$). De Vries characteristics are defined in terms of $C_{deVries}$ and R . Measurements are carried out on a compound adpc042, (b) The simulated molecular structures of the compound adpc042.

A layer shrinkage of 1.7% is calculated from the XRD at a temperature of 13 °C below the SmA^* - SmC^* transition temperature T_{AC} . The layer-shrinkage is small. The behaviour is similar to that in SmA^* phase where the molecular directors in SmA^* phase are distributed on to a cone where the azimuthal angle is degenerated. At the SmA^* to SmC^* transition, the tilt directions condense to within narrower limits, hence the disorder in the azimuthal angle disappears in the SmC^* phase. This process in itself requires no change in the layer thickness.

The reduction factor R of a smectic LC is defined as,

$$R = \frac{\delta(T)}{\theta_{opt}(T=T_{AC})} = \frac{\cos^{-1}(d_c(T)/d_{AC}(T=T_{AC}))}{\theta_{opt}(T=T_{AC})} \quad (1)$$

where $\delta(T)$ governs the layer thickness at a temperature T within SmC^* phase relative to the layer thickness at the SmA^* - SmC^* transition temperature, d_{AC} , on assuming that the rigid rod model is applicable to the LC under investigation [21]. θ_{opt} is the optical tilt angle determined by the POM (Fig. 5). According to Eq. (1), an ideal de Vries smectic with $d_c(T) \approx d_{AC}(T = T_{AC})$ (Fig. 1b) produces a defect-free bookshelf geometry in SmC^* phase with a reduction factor $R = 0$, *i.e.* the short-range molecular tilt order at a lower temperature in the SmA^* phase becomes long range close to the SmA^* - SmC^* transition temperature, where the maximum de Vries cone angle is equal to the saturated optical tilt angle at a temperature close to T_{AC} . On entering the SmC^* from SmA^* phase, the azimuthal ordering of the molecular directors on the cone localizes these on to a single orientation. In this case, the layer contraction is absent and then $d_c/d_{AC} \approx 1$, and therefore $R \approx 0$. Li *et al.* suggested another method of characterizing de Vriesness from measurements of the layer thickness from XRD in terms of the de Vries co-efficient, $C_{deVries}$ [22]. The magnitude of this varies from ‘0’ (classic rigid rod model with a maximum layer shrinkage) to 1 (ideal de Vries SmA^* – SmC^* transition with zero layer shrinkage) such that

$$C_{deVries} = 1 - \left[\frac{(d_{AC} - d_C)}{(d_{AC}(1 - \cos \theta))} \right] \quad (2)$$

The material adpc042 gives rise to $R \approx 0.373$ at 13 °C below the SmA* - SmC* transition temperature. Understandably, R is away from zero but still low, hence the material is close to being a ‘de Vries smectic’. An estimated value of $C_{deVries}$ is ~ 0.86 (Fig. 3 inset) at 13 °C below the SmA* - SmC* transition temperature. The inset plot of Fig. 4 shows that both R and $C_{deVries}$ are almost independent of temperature throughout the entire temperature range of the SmC* phase. The lowest reported value of R so far is 0.17 for the chiral de Vries compound **QL32-6** that exhibits a maximum layer contraction of only 0.2% at 3 °C below the SmA*-SmC* transitions with an optical tilt angle of 20° [13].

C. Electro-optical studies

The birefringence Δn and the apparent optical tilt angle $\theta_{Apparent}$ are determined by recording the intensity of a transmitted beam of light through a LC cell by varying the positions of the polarizer and the analyzer. The procedure involves first keeping **P** fixed, and then rotating the analyzer automatically by various angles. This procedure is repeated for at least three different positions of the polarizer. From the data, Δn and $\theta_{Apparent}$ are calculated. This procedure is different from that given by Park *et al.* [23], who record the transmitted intensity by rotating the sample and also record the transmitted intensity for the P and A (i) parallel and (ii) crossed to each other. The experiment is conducted by applying a triangular signal of frequency 46 Hz and an amplitude of 12 V_{0-peak} μm⁻¹. Frequency of the field is chosen so as to allow sufficient time for the electro-optic switching to occur but to prevent ionic-conductivity contributing to the switching current. An amplitude of the voltage applied to the LC sample adpc042 is large enough so as to make the tilt angle increase slowly with field and then eventually to saturate by the field while avoiding a risk of damage to the sample by the applied electric field.

Figure 5 shows results of the birefringence (Δn) as a function of temperature with and without electric field applied across the cell. On cooling the sample in the absence of field from the isotropic to SmA* phase, the magnitude of Δn first increases slightly, but then starts to decrease within SmA* phase. This decrease in Δn with temperature is due to the de Vries tilt appearing in the SmA* phase and a distribution of the in-layer directors occurring on to the cone. On further cooling the sample in the absence of electric field, Δn suddenly increases

at the $\text{SmA}^* - \text{SmC}^*$ phase transition temperature T_{AC} followed by slow increase with a decrease in temperature. An application of the electric field ($E=12 \text{ V } \mu\text{m}^{-1}$) gives rise to a continuous rise in Δn in the entire temperature range of the SmA^* and SmC^* phases. This field induced increase in Δn is consistent with a change in the interference colors observed by POM (Fig. 3). The behavior is typical of the diffuse-cone model of SmA^* phase with a weak first order $\text{SmA}^* - \text{SmC}^*$ phase transition (Fig. 2b). In the conventional SmA^* of a LC, one may expect a small increase in Δn to occur at the phase transition from a uniaxial SmA^* (with zero tilt angle at $T = T_{AC}$) to a biaxial SmC^* phase.

For adpc042, the measured value of the spontaneous polarization P_S [24] is plotted as a function of the reduced temperature in Fig. 5(b). Measurements are carried out on a $5 \mu\text{m}$ planar cell under the application of a square wave, frequency 110 Hz and large enough amplitude of $12 \text{ V}/\mu\text{m}$. The field is such that the helical structure for temperatures within SmC^* is unwound. It is interesting to note that the field induced polarization is much higher than for conventional ferroelectric liquid crystals. P_S increases with a reduction in temperature below the $\text{SmC}^* - \text{SmA}^*$ transition. The liquid crystalline material under study yields $P_S \sim 82.5 \text{ nC cm}^{-2}$ for $T=(T_{AC} - 30)^\circ\text{C}$.

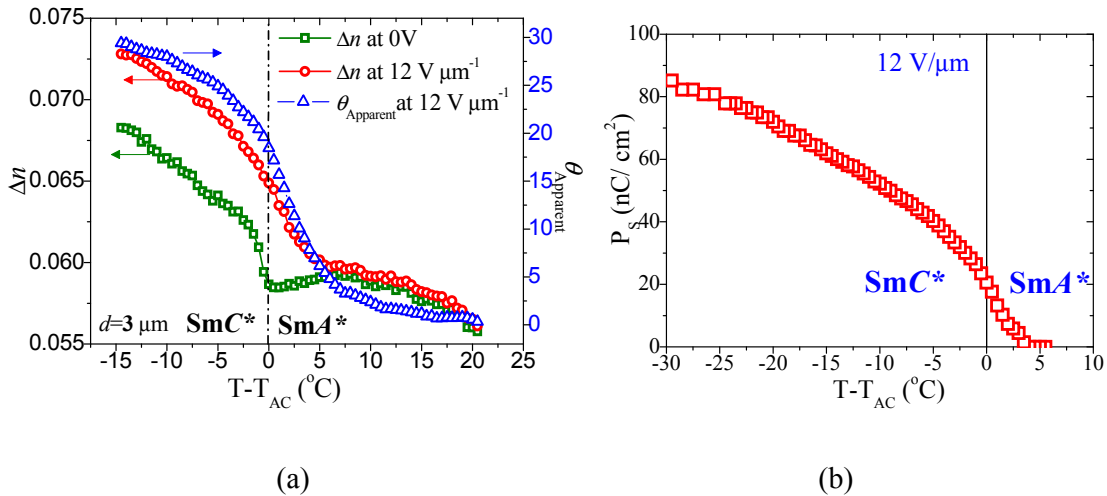


FIG. 5. Results given here are for adpc042. (a) The temperature dependence of the apparent tilt angle (θ_{Apparent}) and the birefringence Δn by applying a maximum field of ($12 \text{ V } \mu\text{m}^{-1}$, red open circles); Δn in the absence of the electric field (green square). Blue triangles denote the apparent tilt angle θ_{Apparent} for a field of $12 \text{ V}/\mu\text{m}$. Measurements are carried out on a $3 \mu\text{m}$ planar-aligned cell filled with adpc042 LC. (b) Spontaneous polarization P_S measured under the cooling process from the isotropic temperature plotted as a function of $(T - T_{AC})$. The measurements are carried out on a $5 \mu\text{m}$ planar cell by applying a square wave AC voltage of $12 [\text{V}_{\text{peak-peak}}/\mu\text{m}]$ at a frequency of 110 Hz.

The measured values of θ_{Apparent} as a function of the electric field for different temperatures in the SmA^* phase are plotted in Fig. 6a. The co-ordinate system and the definition of the various angles are given in Fig. 6b. At a higher temperatures in the SmA^* phase, the magnitude of θ_{Apparent} is low and it increases linearly with the applied field. For temperatures closer to the T_{AC} , θ_{Apparent} becomes nonlinear and it continues to increase slowly up to an electric field of $12 \text{ V } \mu\text{m}^{-1}$ and eventually the tilt angle tends to saturate with the electric field.

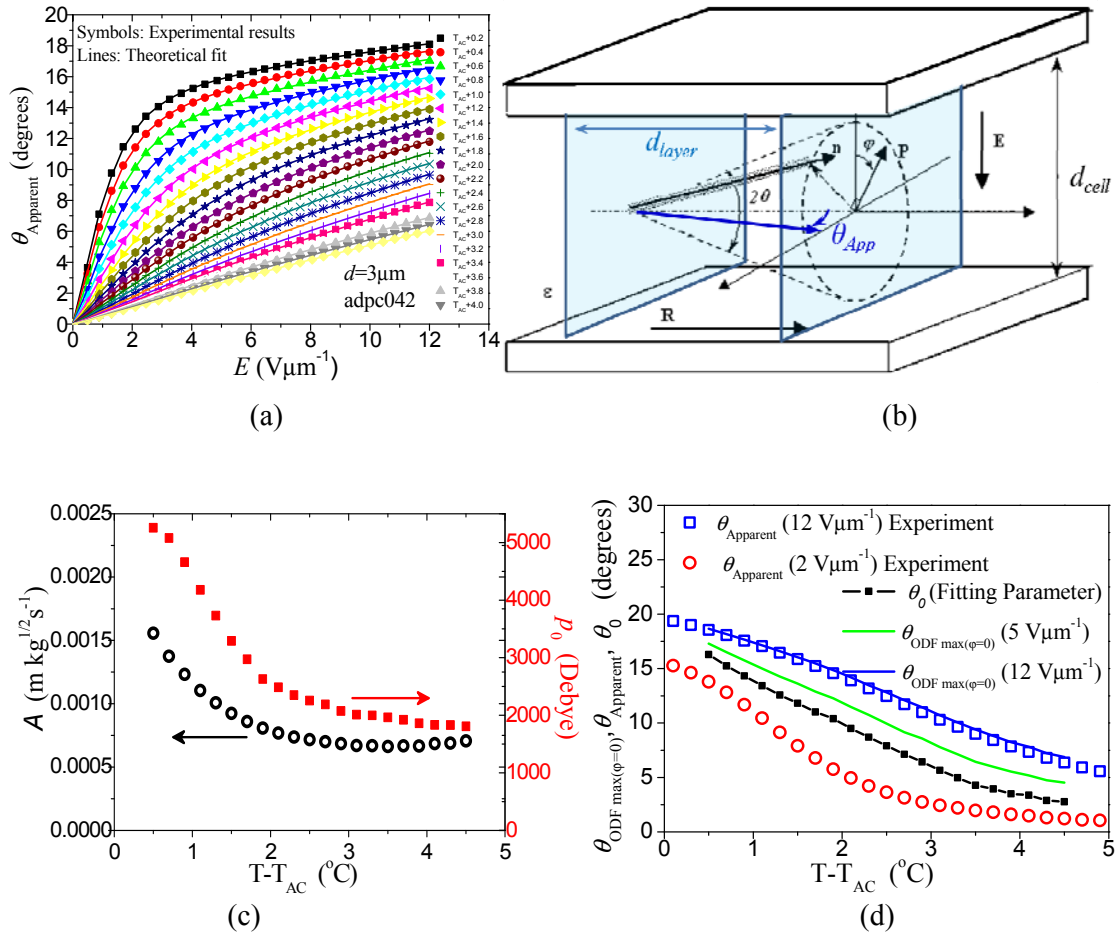


FIG. 6. (a) Variation of the field induced apparent optical tilt θ_{Apparent} (symbols) and the corresponding fitted values (solid lines) for selected temperatures. Measurements are carried out in a $3 \mu\text{m}$ planar cell filled with adpc042 LC. (b) The schematic of the dynamics with the laboratory co-ordinate system (c) Temperature dependence of the model parameters A and p_0 found from the experiments, (d) temperature dependencies of the measured apparent tilt angle θ_{Apparent} (open symbols), the cone angle θ_0 (the line with symbols) apositions of the distribution function of the maxima (lines) for the various electric field strengths applied across a planar-aligned cell.

Several approaches exist in the literature for modeling the unusual electro-optic characteristics of the de Vries smectics [25-30]. The Langevin-Debye model, proposed by

Fukuda [25] in a different context, was used by Clark *et al.* [27] to explain the electro-optical properties of de Vries smectic LCs. This model assumes that for a fixed temperature and zero electric field, the molecular directors in the SmA* phase are tilted but azimuthally distributed on to a cone. In this model, the free energy is expressed as $U = -pE \cos \varphi$, where p is the local dipole moment. However, this model does not correctly explain the dependence of the induced apparent tilt angle (θ_{Apparent} for the electric field) for temperatures rather closer to the SmA*-SmC* transition temperature T_{AC} . In 2013, the Boulder group [28] modified this model where they added an additional term involving the square of the electric field in the expression for the free energy. This is expressed as $U = -p_0 E \sin \theta \cos \varphi (1 + \alpha E \cos \varphi)$. Here, α is the phenomenological scaling factor and $p_0 \sin \theta$ is the dipole moment of the domain correlated in the molecular tilt created by the condensation of azimuthal angles φ . The first term $-p_0 E \sin \theta \cos \varphi$ corresponds to the interaction of the dipole with the field. The second term $-\alpha p_0 E^2 \sin \theta \cos^2 \varphi$ includes the tilt susceptibility that increases with the square of the field E and it leads to a sigmoidal response in both Δn and θ_{Apparent} with E . In this model, the field induced θ_{Apparent} varies between the values inferred from the Δn at zero field (θ_{min}) to the maximum electric field (θ_{max}). These limiting values of θ_{min} and θ_{max} themselves are temperature independent but the actual values within these limits nevertheless are temperature dependent. Therefore, we propose a somewhat different model. This involves three parameters for explaining the electro-optic response where the mean-field free energy is expressed as:

$$U = -p_0 E \sin \theta \cos \varphi + A^2 \sin^2(\theta - \theta_0) \quad (3)$$

Here the first term, $p_0 E \sin \theta \cos \varphi = \mathbf{P} \cdot \mathbf{E}$, describes the usual dipole interaction energy with the field. $|\mathbf{P}|, [= (p_0 \sin \theta)]$, is the magnitude of the dipole moment of a tilt correlated domain. This first term of Eq. (3) is linear in the external electric field E . The second term in this equation defines the cone distribution with a cone aperture angle of $2\theta_0$ and a distribution width proportional to $\sqrt{k_B T}/A$. Here k_B is the Boltzmann constant, T is the absolute temperature and A is the phenomenological co-efficient for the zero field molecular distribution. Note that for the case, $\theta_0 < \sqrt{k_B T}/A$, the model produces “sugar-loaf” ODF (Fig. 7(a)), while a larger θ_0 combined with a narrower distribution width correspond to the “volcano” or “diffuse-cone” distribution (Fig. 7(a)). Thus both scenarios discussed in [31] are reproduced with the same expression for the free energy. Figure 7b illustrates the trend of $[(k_B T/A)^{1/2} - \theta_0]$, as a function of the reduced temperature $(T - T_{\text{AC}})$ for adpc042. One can see

that at 2 to 3 degrees below the phase transition, this function crosses zero. This is a cross-over between the sugar-loaf and the diffuse-cone ODFs.

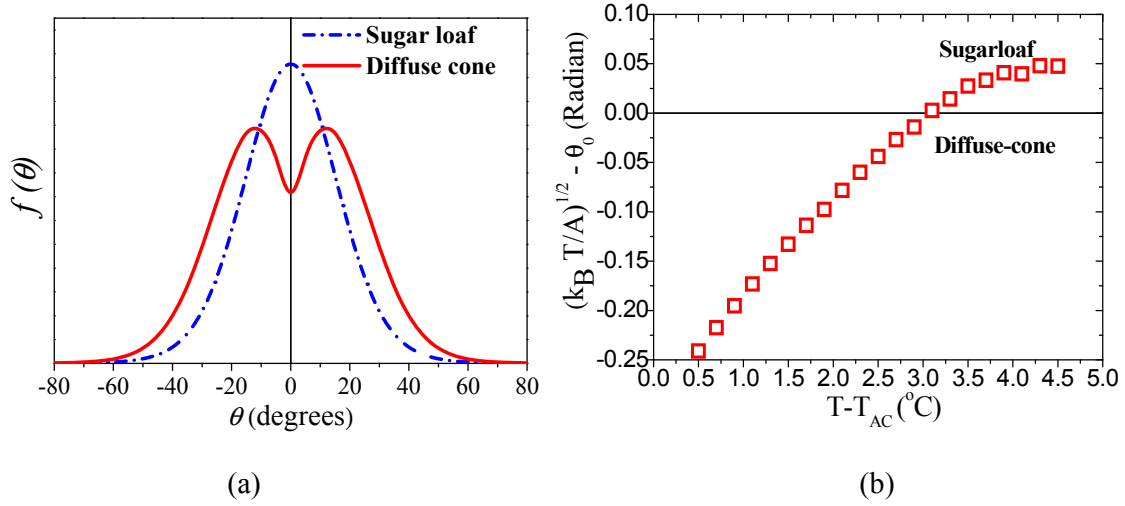


FIG. 7. (a) 2D schematic representation of sugar-loaf (dash-dot lines in blue colour) and diffuse-cone (solid lines in red colour) ODFs. (b) $[(k_B T/A)^{1/2} - \theta_0]$ plotted as a function of the reduced temperature ($T - T_{AC}$). Measurements are carried out on a 3 μm planar cell filled with adpc042.

For the range of the electric fields used, we observe no inflection point in the field dependence of θ_{Apparent} *i.e.* no change in the slope of the derivative of the angle at the point. Therefore, we can achieve a good fit of the experimental data to the model without using terms of higher powers of E .

In order to simulate the behaviour of θ_{Apparent} , we use the mean-field approach combined with equations for the optical response [28]. An average $\langle Y \rangle$ over the orientational distribution can be written as $\langle Y \rangle = \int_0^{2\pi} \int_0^{\pi/2} Y(\theta, \varphi) f(\theta, \varphi) \sin \theta d\theta d\varphi$, where the mean field ODF $f(\theta, \varphi)$ is expressed as:

$$f(\theta, \varphi) = \exp[-U/k_B T] / \int_0^{2\pi} \int_0^{\pi/2} \exp[-U/k_B T] \sin \theta d\theta d\varphi \quad (4)$$

The apparent electro-optical tilt angle θ_{Apparent} is given by:

$$\tan 2\theta_{\text{Apparent}} = \frac{\langle \sin 2\theta \cos \varphi \rangle}{\langle \cos^2 \theta - \sin^2 \theta \cos^2 \varphi \rangle} \quad (5)$$

On fitting the experimentally obtained voltage dependencies of θ_{Apparent} to the above model, we obtain values of p_0 , A and θ_0 each as a function of temperature (Fig. 6c, and 6d). All the parameters tend to increase on approaching T_{AC} as the cell is cooled from the isotropic state to the SmA^* phase. Such an increase is in agreement with the previous models [27, 28].

On using the dipole moment of the correlated domain as $p_0 \approx 5000$ D at 0.5°C above the $\text{SmC}^* - \text{SmA}^*$ phase transition temperature, we can estimate the effective size of a domain using the procedure similar to that adopted by Shen et al. [28]. The effective molecular dipole moment can be estimated from the polarization density measurements performed on a planar-aligned cell in SmC^* phase. In this case P_S is saturated at 69 nC/cm^2 ; $\theta_{\text{Apparent}} = 30^\circ$ at $(T_{\text{AC}} - 19)^\circ\text{C}$, with the molar mass, $M = 590.3 \text{ g/mol}$, density $\rho = 1.2 \text{ g/cm}^3$, the dipole moment is found as $\mu_{\text{eff}} = \frac{P_S M}{\rho N_A \sin \theta_{\text{Apparent}}} \approx 0.34 \text{ D}$. Therefore, the tilt-correlated domain in our experiment contains approximately 6,000 to 15,000 molecules. The effective domain correlation length $\sqrt[3]{\frac{p_0 \sin \theta_{\text{Apparent}}}{P_S}}$, at a temperature close to the $\text{SmA}^* - \text{SmC}^*$ phase transition, is of the order of 30 nm [30].

Parameter A clearly favours the “volcano”- type distribution as illustrated by Fig. 8. A comparison of the cone angle θ_0 that fits the experimentally obtained θ_{Apparent} for different fields is shown in Fig. 6d. Note that for higher field strengths, θ_{Apparent} exceeds θ_0 . This is indicative of a large electro-clinic effect. The solid lines in Fig. 6d show angular positions of the maximum in the ODF simulated for the two electric field strengths (5 and $12 \text{ V}\mu\text{m}^{-1}$) here. The experimental values of θ_{Apparent} for $12 \text{ V}\mu\text{m}^{-1}$ are slightly lower than for an angle for which θ_{ODF} is a maximum. This is expected from a highly distorted diffuse-cone ODF, the distortion is brought about by the applied electric field.

Figures 8a-d show a 3D illustration of the ODF function obtained for a temperature of $(T_{\text{AC}} + 1)^\circ\text{C}$. The ODF is normalized as given below such that its volume for different fields is a constant: $f_{3D} = \frac{f(\theta, \varphi)}{\sqrt[3]{\int_0^{2\pi} \int_0^{\pi/2} f(\theta, \varphi)^3 \sin \theta d\theta d\varphi}}$. Figure 8c shows the cross-section of the ODF in the plane of the LC cell where the maximum of the ODF vs. apparent tilt angle is plotted. The electro-clinic effect for the following electric fields are given in Fig. 8: zero, moderate ($1.3 \text{ V}/\mu\text{m}$) (“cone unwinding”), and for large fields; $12 \text{ V}/\mu\text{m}$ (tilt increases but φ is condensed within a narrow range of values). Note that the modeled ODF shown in Fig. 8 corresponds to the core part of the mesogen that exhibits birefringence at visible wavelengths of light.

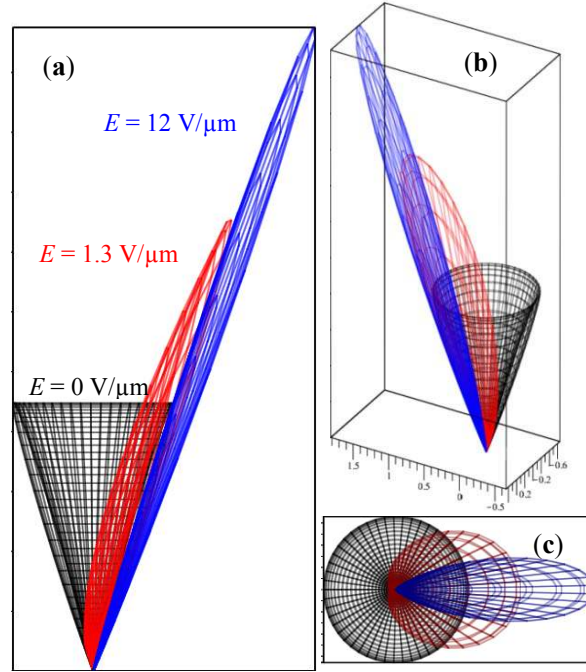


FIG. 8. The ODF of the smectic compound, adpc042, at a temperature of $T = (T_{AC} + 1) ^\circ\text{C}$ for different electric field strengths (0 V, $1.3 \text{ V}\mu\text{m}^{-1}$, and $12 \text{ V}\mu\text{m}^{-1}$). (a-c) are the axonometric projections of $f_{3D}(\theta, \varphi)$.

To test different models, we fit experimental data of θ_{Apparent} as a function of the electric field at a temperature $1 ^\circ\text{C}$ above the $\text{SmA}^* - \text{SmC}^*$ phase transition temperature, T_{AC} (Fig. 9), to the following models: the fixed-angle hollow cone [27], the generalized mean-field model [28] and our 3-parameter mean-field model. For low fields data fitted to the various models is quite adequate. However for the medium and high electric fields, the 3-parameter model shows a closer fit to the experimental data. This is supported by drawing a comparison between sum of the squares of the residuals (χ^2) for the various fits as shown in the inset of Fig. 9. Though, the three models provide reasonable fit to the data, our proposed model has no intrinsic assumption of either the sugar-loaf or the diffuse cone type distribution, i.e. it is not limited to the assumption of a certain ODF in the SmA^* phase. Therefore testing and discrimination among the models is carried out automatically during the fitting procedure. Moreover, the model produces a continuous function for the ODF, having a better physical significance.

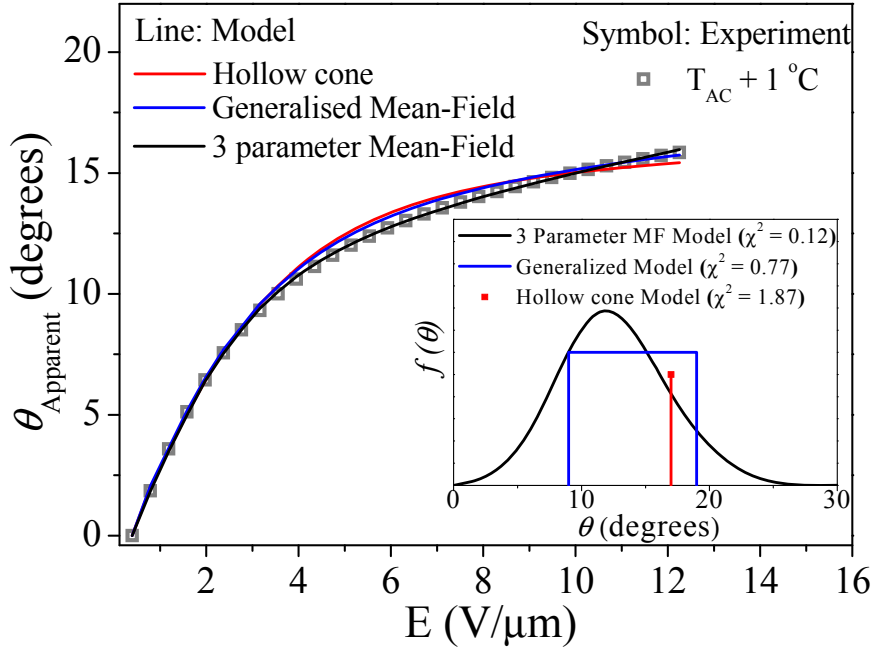


FIG. 9. The experimental, θ_{Apparent} (\square) vs electric field E shown at a temperature of 1°C above the SmA^* - SmC^* phase transition temperature, T_{AC} , are fitted to various models: The hollow cone, the generalized mean Field (MF) and the 3 parameter MF one. A schematic representation of the ODFs for the corresponding three models is given in the inset.

The de Vries LCs normally exhibit large values of the electro-clinic coefficient (denoted by e) [19, 32, 33]. The electro-clinic response is recorded for the material adpc042 in a planar-aligned cell. The experiment is carried out by keeping the smectic layer normal at an angle of 22.5° with respect to the polarizer. The light intensity I , transmitted through the LC cell, in the absence of the field E is given by:

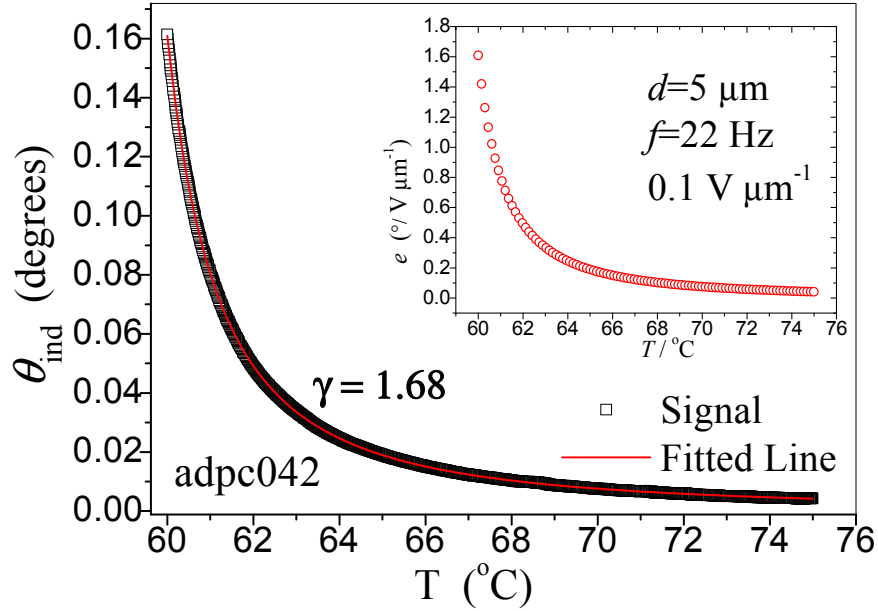
$$I = I_0 \sin^2(2\alpha) \sin^2(\pi \Delta n d / \lambda) \quad (6)$$

I_0 is the incident intensity, α is the angle between the molecular director and the polarizer, Δn is the birefringence, d is the cell thickness, and λ is the wavelength of the incident light. When an electric field is applied across the cell, the transmitted intensity varies linearly with the induced tilt angle $\delta\alpha = \theta_{\text{ind}}$. Differentiating Eq. (6) with respect to α is given as:

$$\delta I = 2I_0 \sin(4\alpha) \sin^2(\pi \Delta n d / \lambda) \theta_{\text{ind}} \quad (7)$$

From Eqns. (6) and (7) and for $\alpha = 22.5^\circ$ we obtain $\theta_{\text{ind}} = \delta I / 4I$. Figure 10 shows θ_{ind} as a function of temperature over the temperature range of SmA^* phase. The magnitude of θ_{ind}

418 increases with decreasing temperature. On approaching, T_{AC} , from the high temperature side
 419 of SmA^* , magnitude of θ_{ind} diverges and this corresponds to the divergence of the correlation
 420 length of the tilt domain and here the azimuthal angle is condensed to lie within narrower
 421 limits.



422

423 **FIG. 10.** The temperature dependence of electro-clinic response θ_{ind} of adpc042 (\square):
 424 experimental value, red line (—): fitting to Eq. (7). The inset figure is the electro-
 425 clinic co-efficient e (red open circle \square) calculated using the Eq. $e = \theta_{ind}/E$ as a
 426 function of temperature. Experiments were conducted under cooling within the
 427 temperature range of SmA^* phase up to a temperature of $T = (T_{AC} + 1)^\circ C$ by the
 428 application of $0.1 V_{0-peak} \mu m^{-1}$ (planar aligned cell, $d=5 \mu m$ sine wave AC voltage of
 429 22 Hz).

430 The amplitude of θ_{ind} with temperature can be expressed by the power law equation as
 431 follows [34]

$$432 \quad \theta_{ind} = \frac{C}{(T - T_{AC})^\gamma} \quad (8)$$

433 Here C is the scaling constant, T_{AC} is the SmA^* - SmC^* transition temperature and γ is the
 434 critical exponent. For the smectic material under investigation $\gamma = 1.68$. For a conventional
 435 SmA^* - SmC^* transition, γ is 1.33 [35]. Values of γ greater than 1.33 reflect the short-range
 436 correlation of molecular directors in three dimensions, again a characteristic of the de Vries
 437 smectics. The inset plot in Fig. 10 shows the temperature dependence of the electroclinic co-
 438 efficient e , calculated from the definition of $e = \theta_{ind}/E$.

D. Dielectric Spectroscopy

Figure 11a shows a three dimensional plot of temperature dependent dielectric loss spectra (ε'') of a planar aligned cell filled with the material adpc042 LC. Note that the temperature independent high frequency process is due to the resistance of ITO in series with the capacitance of the filled cell. The relaxation process in the SmA* phase corresponds to fluctuation of the tilt angle and this mode is known as the soft mode (SM). This arises mainly as the system approaches T_{AC} the elastic constant controlling the tilt fluctuations decreases or gets softer. The low frequency dielectric relaxations in the SmC* phase is associated with the Goldstone (GM) mode in which the molecular director is subjected to continual symmetry breaking.

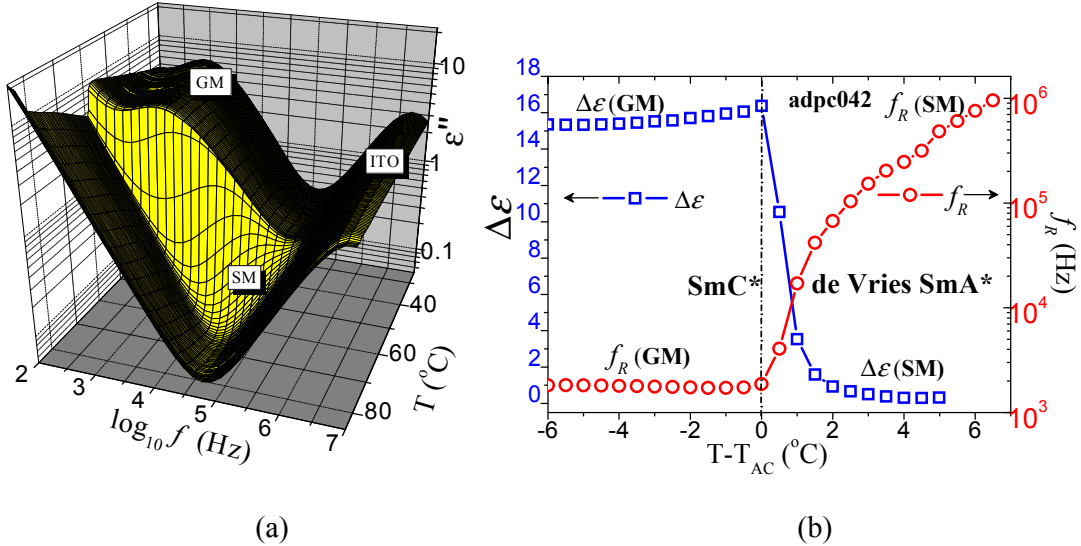


FIG. 11. (a) A 3-D plot of temperature dependent dielectric loss spectra (ε'') of the compound adpc042 (cell thickness, $d=10 \mu\text{m}$) in a planar-aligned cell. The dielectric measurements are carried out under cooling. Temperature stabilization is 0.05°C and the applied voltage is $0.1 V_{\text{rms}}$ (b) Dielectric strength $\Delta\varepsilon$ (open blue squares \square) and the corresponding relaxation frequency f_R (red open circles \circ) as a function of temperature. SM and GM refer to the soft and Goldstone modes, respectively.

The dielectric spectra are analysed using the Novocontrol WINFIT programme. The temperature dependent dielectric strength $\Delta\varepsilon$ and the relaxation frequency f_R are obtained by fitting the dielectric spectra to the Havriliak-Negami Eq. [36]:

$$\varepsilon^*(\omega) = \varepsilon' - i\varepsilon'' = \varepsilon_\infty + \sum_{j=1}^n \frac{\Delta\varepsilon_j}{[1 + (i\omega\tau_j)^{\alpha_j}]^{\beta_j}} - \frac{i\sigma_{dc}}{\varepsilon_0\omega} \quad (9)$$

where, ε_∞ is the high frequency permittivity depending on the electronic and atomic polarizability, j is the number of relaxation processes which varies from 1 to n , $\omega=2\pi f$ is the angular frequency in radians, ε_0 is the free space permittivity, τ_j is relaxation time of the j^{th} process, $\Delta\varepsilon_j$ is the dielectric strength and α_j and β_j are the symmetric and asymmetric broadening parameters of the j^{th} dielectric relaxation process related to the distribution of relaxation times. The term $(-i\sigma_{dc}/\varepsilon_0\omega)$ gives the dielectric loss due to the ionic conduction at and is dominant at lower frequencies due to the inverse ω term. The relaxation frequency f_j of the j^{th} process is related to τ_j as [37]:

$$f_j = \frac{1}{2\pi\tau_j} \left[\sin\left(\frac{\alpha_j\pi}{2+2\beta_j}\right) \right]^{1/\alpha_j} \left[\sin\left(\frac{\alpha_j\beta_j\pi}{2+2\beta_j}\right) \right]^{-1/\alpha_j} \quad (10)$$

The temperature dependencies of $\Delta\varepsilon$ and f_R are shown in Fig. 11b. The amplitude of $\Delta\varepsilon$ shows a pronounced increase when the system approaches T_{AC} from the SmA^* phase. The maximum value of $\Delta\varepsilon$ at T_{AC} is 16.8. The corresponding f_R is decreasing in the SmA^* phase with a sharper trend in its lower temperature range. Remarkably strong soft mode dielectric absorption is observed in the dielectric spectra of de Vries LCs in contrast to the compounds that exhibit a conventional SmA^* [38-41].

IV. CONCLUSION

We have designed and synthesised two 5-phenyl pyrimidine derivatives with siloxane and fluorocarbon chain terminations, both with a chiral (*R,R*)-2,3-epoxyhexoxy side chain. Mesophases formed by these compounds are investigated using a number of techniques: DSC, POM, XRD, electro-optical, and dielectric spectroscopy.

We find that the maximum layer contraction for the siloxane terminated adpc042 at a temperature of 13 °C below the SmA^* - SmC^* transition is 1.7% and a reduction factor R is 0.37 on a scale of 1 to 0. This compound is considered to be a good “de Vries smectic” with the de Vries coefficient $C_{deVries}$ of 0.86 on the scale of 0 to 1. The soft mode dielectric relaxation strength $\Delta\varepsilon$ shows a critical behaviour when the system approaches SmA^* - SmC^* transition from the high temperature side. The critical exponent of the electro-clinic response is found to be $\gamma = 1.68$. Value of the exponent is much greater than 1.33, found for most conventional smectics. Temperature dependence of the correlation length suggests that the material has de-Vries characteristics.

We introduce a three parameter MF model for describing the ODF of the molecular director in SmA* phase with a view of fitting the field-induced experimental apparent tilt angle θ_{Apparent} data as a function of the electric field. Close to the SmA* - SmC* transition temperature, the birefringence in SmA* phase is seen to decrease with a reduction in temperature. This is due to the emergence of a non-zero value of cone angle θ_0 , the magnitude of which increases to 17° as the SmA*-SmC* phase transition is approached. The proposed model fits the experimental data on apparent tilt angle and leads to the diffuse-cone ODF, at temperatures close to the phase transition temperatures. However θ_0 decreases with an increase in temperature and the ODF displays a cross over from the diffuse-cone to the sugar loaf at ~ 3.5 °C above T_{AC} .

Acknowledgements

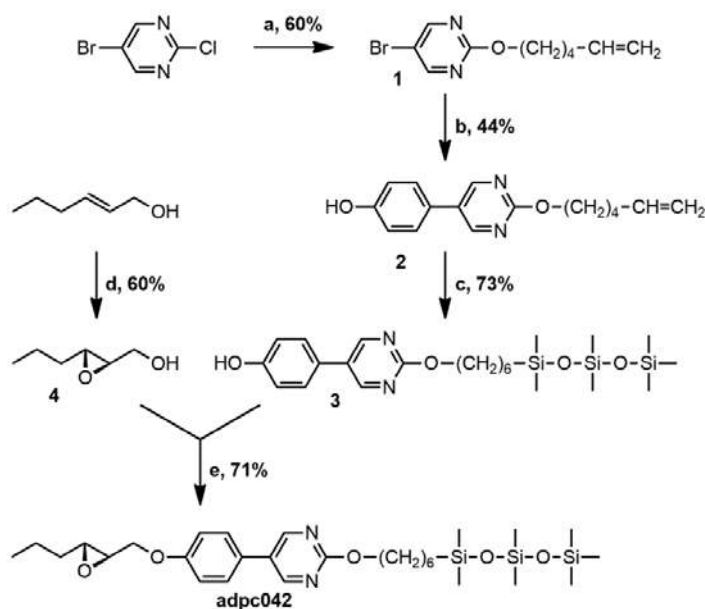
Work was supported by 13/US/I2866 from the Science Foundation Ireland as part of the US-Ireland Research and Development Partnership program jointly administered with the United States National Science Foundation under grant number NSF-DMR-1410649. Financial support for the Belfast group was from the Department for Employment and Learning under with grant code USI 056. X-ray measurements were done in Warsaw, under the EU Cost ICI 1208 2014-17 project. We thank Professor Satyendra Kumar for co-ordinating the US-Ireland project.

APPENDIX: SYNTHETIC PROCEDURE

All reagents were purchased from Sigma Aldrich, Fluorochem, Alfa Aesar, ABCR, Synthonix and used without any further purification. Solvents were purchased from Sigma Aldrich, DMF was purchased pre-dried, THF was dried using a sodium/benzophenone still under N₂ and DCM was dried using CaH₂. All reactions were generally carried out under argon using oven-dried glassware. TLC plates were performed on Merck silica gel 60 F₂₅₄ and were visualized using a 254 nm light source. Flash column chromatography was performed on Fluorochem silica gel 60 (40-63 micron).

IR spectra were recorded using a Perkin Elmer Spectrum Two FT-IR spectrometer. ¹H and ¹³C spectra were recorded at 25°C (CDCl₃ as solvent and TMS as reference) using a Bruker 400 MHz Ultrashield (Avance 400). HRMS spectra were recorded using a Waters – TOF Electrospray micromass LCT premier. Optical rotations were recorded using a polarimeter Perkin Elmer: model 341 Polarimeter.

521 The synthesis of adpc042 was carried out through the scheme shown in FIG. 12.

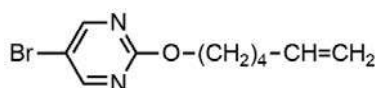


522

523 **FIG. 12.** General scheme for the preparation of **adpc042**

524 Further details of synthesis and characterization of each stage of intermediates are given
525 below:

526 The chemical structure of compound 1 is given in Fig. 13.



527

528 **FIG. 13.** Chemical structure of compound **1**

529 5-Hexen-1-ol (0.62 g, 6.2 mmol) was dissolved in dry toluene (15 mL) and sealed in a
530 schlenk under argon. Sodium (0.16 g, 7.00 mmol) was added as a solid and the solution was
531 stirred at 50 °C overnight. 5-Bromo-2-chloropyrimidine (1.00 g, 5.17 mmol) was added and
532 the solution stirred for 8 hours at 50 °C. The solution was filtered, water (20 mL) was added
533 and the crude extracted with ethyl acetate (3 x 30 mL). The product was purified by column
534 chromatography (ethyl acetate: hexane, 1:9, $R_f = 0.45$) to yield a colourless oil (0.80 g, 3.11
535 mmol, 60%).

536 $^1\text{H NMR}$ (400 MHz, CDCl_3) δ : 8.51 (s, 2H), 5.81 (ddt, $J = 6.67, 6.67, 10.18, 16.91$, H), 4.98
537 (m, 2H), 4.33 (t, $J = 6.60$, 2H), 2.12 (m, 2H), 1.82 (m, 2H), 1.57 (m, 2H).

¹³C NMR (101 MHz, CDCl₃) δ: 164.15 (C), 159.75 (2CH), 138.59 (CH), 115.01 (CH₂), 111.79 (C), 68.42 (CH₂), 33.55 (CH₂), 28.36 (CH₂), 25.36 (CH₂).

IR (film): $\tilde{\nu}$ = 3076, 2936, 1640, 1570, 1432, 1332, 1176, 1122, 1024, 912, 794 cm⁻¹.

HRMS (EI): m/z calcd for C₂₀H₂₇N₄O₂Br₂ [2M + H⁺] 513.0501, found: 513.0513.

The chemical structure of the compound **2** in Fig. 10 is given in Fig. 14 and the synthesis and characterization are detailed below:

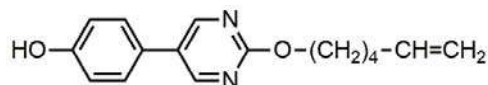


FIG. 14. Chemical structure of compound **2**

4-hydroxyphenylboronic acid (0.32 g, 2.33 mmol) and **1** (0.50 g, 1.94 mmol) were sealed in a schlenk under argon. Toluene (12 mL) was added and the solution degassed for 5 minutes. Degassed methanol (7 mL) and potassium carbonate dissolved in degassed water (3 mL) were added to the schlenk. Tetrakis(triphenylphosphine)palladium(0) (0.11 g, 0.10 mmol) was added as a solid and the solution was refluxed overnight. The crude was concentrated and water (30 mL) was added before extraction with DCM (3 x 30 mL). The organic phase was dried with magnesium sulphate and concentrated in vacuo. The product was purified by column chromatography (ethyl acetate: DCM, 15:85, where R_f = 0.57 in ethyl acetate: hexane, 1:1) to yield a white solid (0.23 g, 0.85 mmol, 44%).

¹H NMR (400 MHz, CDCl₃) δ: 8.66 (s, 2H), 7.90 (s, 1H), 7.37 (d, *J* = 8.72, 2H), 7.03 (d, *J* = 8.71), 5.79 (ddt, *J* = 6.65, 6.65, 10.18, 16.91, 1H), 4.97 (m, 2H), 4.42 (t, *J* = 6.58, 2H), 2.11 (m, 2H), 1.85 (m, 2H), 1.58 (m, 2H).

¹³C NMR (101 MHz, CDCl₃) δ: 164.22 (C), 157.17 (C), 156.95 (2CH), 138.61 (CH), 128.48 (C), 127.98 (2CH), 126.19 (C), 116.73 (2CH), 114.97 (CH₂), 68.06 (CH₂), 33.55 (CH₂), 28.48 (CH₂), 25.38 (CH₂).

IR (film): $\tilde{\nu}$ = 3099, 3022, 2950, 1602, 1558, 1434, 1326, 1270, 1180, 1072, 924, 834 cm⁻¹.

HRMS (EI): The molecular weight for C₁₆H₁₉N₂O₂ [M + H⁺] was calculated as 271.1447 and found to be 271.1446.

The chemical structure of compound **3** is given in Fig. 15; synthesis and characterization are detailed below:

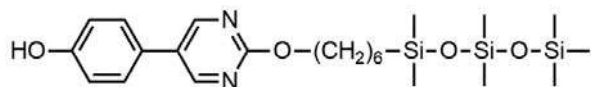


FIG. 15. Chemical structure of compound **3**

2 (0.22 g, 0.81 mmol) was dissolved in dry THF (12 mL) under argon. 1,1,1,3,3,5,5-heptamethyltrisiloxane (0.35 g, 1.59 mmol) and platinum(0)-1,3-divinyl-1,1,3,3-tetramethyldisiloxane (0.20 mL of 0.1M solution, 0.02 mmol) were added to the flask and the solution was stirred for 2 hours. The crude is concentrated and purified by column chromatography (ethyl acetate: hexane, 2:8, where $R_f = 0.30$ in ethyl acetate: hexane, 3:7) to yield a colourless wax (0.29 g, 0.59 mmol, 73%).

^1H NMR (400 MHz, CDCl_3) δ : 8.65 (s, 2H), 7.39 (d, $J = 8.70$), 6.96 (d, $J = 8.72$, 2H), 5.37 (s, 1H), 4.39 (t, $J = 6.72$), 1.83 (m, 2H), 1.42 (m, 6H), 0.54 (m, 2H), 0.08 (s, 9H), 0.06 (s, 6H), 0.02 (s, 6H).

^{13}C NMR (101 MHz, CDCl_3) δ : 164.71 (C), 157.08 (CH), 156.18 (C), 128.11 (CH), 128.08 (C), 127.30 (C), 116.48 (CH), 68.19 (CH_2), 33.36 (CH_2), 29.07 (CH_2), 25.91 (CH_2), 23.39 (CH_2), 18.47 (CH_2), 2.04 (3CH_3), 1.50 (2CH_3), 0.41 (3CH_3).

IR (film): $\square = 2958, 1600, 1442, 1332, 1258, 1048, 840 \text{ cm}^{-1}$.

HRMS (EI): m/z calcd for $\text{C}_{23}\text{H}_{41}\text{N}_2\text{O}_4\text{Si}_3$ [$\text{M} + \text{H}^+$] 493.2374, found: 493.2379.

The chemical structure of compound **4** is given in Figure **16** and other details are followed below:



FIG. 16. Chemical structure of compound **4**

Trans-2-hexen-1-ol (1.00 g, 9.98 mmol), Shi Epoxidation Diketal Catalyst (0.77 g, 3.00 mmol) and Tetrabutylammonium hydrogensulfate (0.06 g, 0.18 mmol) were dissolved in dimethoxymethane/acetonitrile (100 mL, 2:1). Acetic acid (0.35 mL) was added to potassium carbonate (70 mL of 0.1M solution) and this was added to the reaction which was then cooled to -10°C . Oxone (8.48 g, 13.78 mmol) was dissolved in ethylenediaminetetraacetic acid disodium salt (50 mL of 0.004M solution in water) and potassium carbonate (8.00 g, 57.91 mmol) was dissolved in water (50mL). The oxone and the carbonate solution were added to the reaction flask dropwise over 3 hours while keeping the temperature below 0°C . Water was added and the organic phase extracted with DCM (3 x 50 mL) before drying with magnesium sulphate and concentrating the solution. The epoxide was purified by column chromatography (hexane: diethyl ether, 2:1 \rightarrow 100% ether once product appears, $R_f = 0.53$ in

DCM: ethyl acetate, 1:1) to yield a colourless oil (0.70 g, 5.99 mmol, 60%). The column was compacted using hexane: diethyl ether, 2:1 and 1% triethylamine to neutralize the silica.

¹H NMR (400 MHz, CDCl₃) δ : 3.91 (ddd, J = 2.58, 5.58, 12.53, 1H), 3.63 (ddd, J = 4.30, 7.29, 12.52), 2.96 (td, J = 2.36, 5.50, 5.65, 1H), 2.92 (m, 1H), 1.74 (m), 1.50 (m, 3H), 0.96 (t, J = 7.26, 3H).

¹³C NMR (101 MHz, CDCl₃) δ : 61.93 (CH₂), 58.55 (CH), 56.01 (CH), 33.78 (CH₂), 19.47 (CH₂), 14.10 (CH₃).

IR (film): ν = 3418, 2962, 2874, 1650, 1464, 1382, 1220, 1046, 900, 849 cm⁻¹.

$[\alpha]_D^{20}$: +38.75 (c 0.022, CHCl₃).

The chemical structure of adpc042 is given in Fig. 17 and other details are followed below:

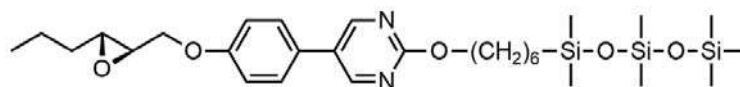


FIG. 17. Chemical structure of compound **adpc042**

3 (0.56 g, 1.14 mmol), **4** (0.12 g, 1.03 mmol) and triphenylphosphine (0.33 g, 1.26 mmol) were dissolved in dry THF (20 mL) under argon. Diethyl azodicarboxylate (0.22 g, 1.24 mmol) was dissolved in dry THF (8 mL) under argon before being added dropwise to the reaction flask. The flask was stirred overnight and then concentrated. The product was purified by column chromatography (ethyl acetate: hexane, 1:9, where R_f = 0.60 in ethyl acetate: hexane, 3:7) to yield a white wax (0.43 g, 0.73 mmol, 71%).

¹H NMR (400 MHz, CDCl₃) δ : 8.65 (s, 2H), 7.43 (d, J = 8.81, 2H), 7.02 (d, J = 8.81, 2H), 4.38 (t, J = 6.71, 2H), 4.23 (dd, J = 3.34, 11.08, 1H), 4.02 (dd, J = 5.52, 11.08), 3.13 (ddd, J = 2.29, 3.27, 5.53, 1H), 2.98 (td, J = 2.20, 5.53, 5.64, 1H), 1.83 (m, 2H), 1.65-1.30 (m, 10H), 0.99 (t, J = 7.28), 0.54 (m, 2H), 0.08 (s, 9H), 0.06 (s, 6H), 0.01 (s, 6H).

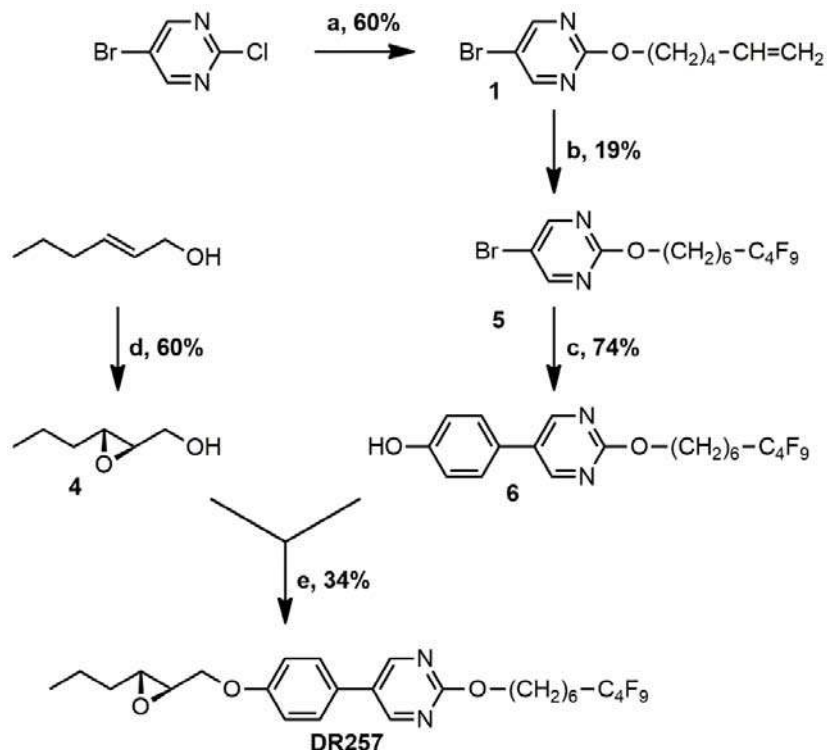
¹³C NMR (101 MHz, CDCl₃) δ : 164.76 (C), 158.92 (C), 157.10 (2CH), 127.95 (C), 127.89 (2CH), 127.68 (C), 115.71 (2CH), 68.82 (CH₂), 68.15 (CH₂), 56.66 (CH), 56.22 (CH), 33.84 (CH₂), 33.36 (CH₂), 29.06 (CH₂), 25.91 (CH₂), 23.39 (CH₂), 19.44 (CH₂), 18.46 (CH₂), 14.10 (CH₃), 2.04 (3CH₃), 1.50 (2CH₃), 0.40 (2(CH₃)).

IR (film): ν = 2958, 1598, 1548, 1448, 1256, 1048, 840 cm⁻¹.

HRMS (EI): m/z calcd for C₂₉H₅₁N₂O₅Si₃ [M + H⁺] 591.3096, found: 591.3097.

$[\alpha]_D^{20}$: +9.74 (c 0.029, CHCl₃).

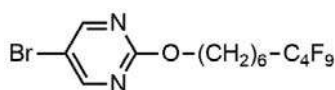
626 The synthesis of DR257 was carried out through the scheme shown in FIG. 18, further details
 627 of each stage are provided below.



628

629 **FIG. 18.** General scheme for the preparation of **DR257**

630 Synthesis and characterization of the intermediates are given below. Structure of the
 631 compound **5** is given in Fig. 19 and details follow below:



632

633 **FIG. 19.** The Chemical structure of compound **5**

634 $\text{Na}_2\text{S}_2\text{O}_4$ (0.040 g, 0.230 mmol) and Na_2HPO_4 (0.039 g, 0.276 mmol) were added to a
 635 mixture of 1-iodoperfluorobutane (0.955 g, 2.76 mmol), the alkene **1** (0.590 g, 2.30 mmol) in
 636 $\text{H}_2\text{O}/\text{CH}_3\text{CN}$ (12 mL 1:3) [42]. The mixture was stirred overnight at room temperature. Et_2O
 637 and H_2O were added to the mixture and the phases were separated. The organic phase was
 638 extracted with Et_2O (2 X 10 mL) and the combined organic phase was dried with magnesium
 639 sulphate. The solvent was removed at reduce pressure to led a yellow oil. This iodinated
 640 intermediate was used without further purification. Bu_3SnH (0.802 g, 2.76 mmol) and a
 641 catalytic amount of AIBN (12 mg) were added to the oil. The reaction mixture was heated to

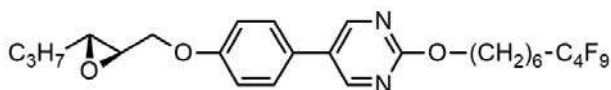


FIG. 21. Chemical structure of compound **DR257**

6 (0.220 g, 0.449 mmol), **4** (0.048 g, 1.03 mmol) and triphenylphosphine (0.129 g, 0.490 mmol) were dissolved in dry THF (10 mL) under argon. Diethyl azodicarboxylate (0.085 g, 0.490 mmol) was dissolved in dry THF (4 mL) under argon before being added dropwise to the reaction flask. The flask was stirred overnight and then concentrated. The product was purified by column chromatography (ethyl acetate: hexane, 1.5:9, where $R_f = 0.60$ in ethyl acetate: hexane, 3:7) to yield a white powder (0.82 g, 0.140 mmol, 34%).

^1H NMR (400 MHz, CDCl_3) δ : 8.65 (s, 2H), 7.42 (m, 2H), 7.01 (m, 2H), 4.39 (t, $J = 6.5$, 2H), 4.23 (dd, $J = 11.1$, 3.3, 1H), 4.01 (dd, $J = 11.1$, 5.5, 1H), 3.12 (m, 1H), 2.97 (m, 1H), 2.06 (m, 2H), 1.90 – 1.80 (m, 2H), 1.69 – 1.40 (m, 10H), 0.98 (t, $J = 7.3$, 3H).

^{13}C NMR (101 MHz, CDCl_3) δ : 164.63 (C), 158.94 (C), 157.09 (2CH), 128.08 (C), 127.87 (2CH), 127.56 (C), 115.70 (2CH), 68.81 (CH_2), 67.72 (CH_2), 56.61 (CH), 56.20 (CH), 33.81 (CH_2), 30.91 (t, $J = 22.3$, CH_2), 29.02 (CH_2), 28.84 (CH_2), 25.88 (CH_2), 20.25 (t, $J = 3.7$, CH_2), 19.41 (CH_2), 14.06 (CH_3).

^{19}F NMR (376 MHz, CDCl_3) δ : -81.08, -114.63, -124.52, -126.08.

HRMS (EI): m/z calcd for $\text{C}_{26}\text{H}_{30}\text{F}_9\text{N}_2\text{O}_3$ [$\text{M} + \text{H}^+$] 589.2097, found 589.2104.

$[\alpha]_D^{20}$: +8.868 (c 0.0106, CHCl_3).

References:

- [1] N. A. Clark and S. T. Lagerwall, *Appl. Phys. Lett.* **36**, 899 (1980).
- [2] S. T. Lagerwall, *Ferroelectric and Antiferroelectric Liquid Crystals*, Wiley-VCH, Weinheim (1999).
- [3] T. P. Rieker, N. A. Clark, G. S. Smith, D. S. Parmar, E. B. Sirota and C. R. Safinya, *Phys. Rev. Lett.* **59**, 2658 (1987).
- [4] J. P. Lagerwall and F. Giesselmann, *Chem. Phys. Chem.* **7**, 20 (2006).
- [5] M. V. Gorkunov, F. Giesselmann, J. P. F. Lagerwall, T. J. Sluckin and M. A. Osipov, *Phys. Rev. E* **75**, 060701 (2007).
- [6] M. V. Gorkunov, M. A. Osipov, J. P. F. Lagerwall and F. Giesselmann, *Phys. Rev. E* **76**, 051706 (2007).
- [7] K. Saunders, D. Hernandez, S. Pearson and J. Toner, *Phys. Rev. Lett.* **98**, 197801 (2007).

- 703 [8] K. Saunders, Phys. Rev. E **77**, 061708 (2008).
- 704 [9] V. Swaminathan, V. P. Panov, Yu. P. Panarin, S. P. Sreenilayam, J. K. Vij, A. Panov, D.
705 Rodriguez-Lojo, P. J. Stevenson, and E. Gorecka, Liq. Cryst., <https://doi.org/10.1080/02678292.2017.1359694> (2017).
- 706
- 707 [10] H. G. Yoon, D. M. Agra-Kooijman, K. Ayub, R. P. Lemieux, and S. Kumar, Phys. Rev.
708 Letts., **106**, 087801(2011); D. M. Agra-Kooijman, H. G. Yoon, S. Dey, and S. Kumar,
709 Phys. Rev. E **89**, 032506 (2014).
- 710 [11] Y. Gao, J. M. Klunder, R. M. Hanson, H. Masamune, S. Y. Ko, and K. B. Sharpless, J.
711 Am. Chem. Soc. **109**, 5765 (1987); Y. Tu, Z. Wang, and Y. Shi, J. Am. Chem. Soc. **118**,
712 9806 (1996).
- 713 [12] D. Nonnenmacher, M. A. Osipov, J. C. Roberts, R. P. Lemieux, and F. Giesselmann,
714 Phy. Rev. E **82**, 031703 (2010).
- 715 [13] C. P. J. Schubert, C. Muller, F. Giesselmann, and R. P. Lemieux, J. Mater. Chem. C **4**,
716 8483 (2016).
- 717 [14] J. C. Roberts, N. Kapernaum, Q. Song, D. Nonnenmacher, K. Ayub, F. Giesselmann,
718 and R. P. Lemieux, J. Am. Chem. Soc. **132**, 364 (2010).
- 719 [15] C. P. J. Schubert, A. Bogner, J. H. Porada, K. Ayub, T. Andrea, F. Giesselmann, and R.
720 P. Lemieux, J. Mater. Chem. C **2**, 4581 (2014).
- 721 [16] A. de Vries, J. Chem. Phys. **71**, 25 (1979).
- 722 [17] G. W. Gray and J. W. Goodby, *Smectic Liquid Crystals*, Leonard Hill, London (1984).
- 723 [18] A. de Vries, Mol. Cryst. Liq. Cryst. **41**, 27 (1977).
- 724 [19] J. W. Goodby, Ch. 3, *Handbook of Liquid Crystals*, Volume 1, 2nd ed., Wiley-VCH
725 (2015) [editors: J. W. Goodby, P. J. Collings, T. Kato, C. Tschierske, H. F. Gleeson, P.
726 Raynes]
- 727 [20] J. Naciri, G. P. Crawford, B. R. Ratna, and R. Shashidhar, Ferroelectrics **148**, 297
728 (1993).
- 729 [21] Y. Takanishi, Y. Ouchi, H. Takezoe, A. Fukuda, A. Mochizuki, and M. Nakatsuka, Jpn.
730 J. Appl. Phys. **29**, L984 (1990).
- 731 [22] L. Li, C. D. Jones, J. Magolan, and R. P. Lemieux, J. Mater. Chem. **17**, 2313 (2007).
- 732 [23] B. Park, S. -S. Seomun, M. Nakata, and M. Takahashi, Jpn. J. Appl. Phys. **38**, 1474
733 (1999).
- 734 [24] V. M. Vaksman and Yu. P. Panarin, Mol. Mater. **1**, 147 (1992); V. Panov, J. K. Vij, and
735 N. M. Shtykov, Liq. Cryst. **28**, 615 (2001).
- 736 [25] S. Inui, N. Iimura, T. Suzuki, H. Iwane, K. Miyachi, Y. Takanishi, and A. Fukuda, J.
737 Mater. Chem. **6**, 671 (1996).
- 738 [26] S. Garoff and R. B. Meyer, Phys. Rev. Lett. **38**, 848 (1977).

739 [27] N. A. Clark, T. Bellini, R.-F. Shao, D. Coleman, S. Bardon, D. R. Link, J. E. MacLennan,
740 X.-H. Chen, M. D. Wand, D. M. Walba, P. Rudquist, and S. T. Lagerwall, *Appl. Phys.*
741 *Lett.* **80**, 4097 (2002).

742 [28] Y. Shen, L. Wang, R. Shao, T. Gong, C. Zhu, H. Yang, J. E. MacLennan, D. M. Walba,
743 and N. A. Clark, *Phys. Rev. E* **88**, 062504 (2013).

744 [29] S. T. Lagerwall, P. Rudquist, and F. Giesselmann, *Mol. Cryst. Liq. Cryst.* **510**, 148
745 (2009).

746 [30] J. V. Selinger, P. J. Collings, and R. Shashidhar, *Phys. Rev. E* **64**, 061705 (2001).

747 [31] R. Qiu, J. T. Ho, and S. K. Hark, *Phys. Rev. A* **38**, 1653 (1988).

748 [32] F. Giesselmann, P. Zugenmaier, I. Dierking, S. T. Lagerwall, B. Stebler, M. Kaspar, V.
749 Hamplova, and M. Glogarova, *Phys. Rev. E* **60**, 598 (1999).

750 [33] O. E. Panarina, Yu. P. Panarin, J. K. Vij, M. S. Spector, and R. Shashidhar, *Phys. Rev. E*
751 **67**, 051709 (2003).

752 [34] K. L. Sandhya, Yu. P. Panarin, V. P. Panov, J. K. Vij, and R. Dabrowski, *Eur. Phys. J. E*
753 **27**, 397 (2008).

754 [35] P. G. de Gennes and J. Prost, *The Physics of Liquid Crystals*, Clarendon, Oxford (1993).

755 [36] S. Havriliak (Jr.) and S. Negami, *Polymer* **8**, 161 (1967).

756 [37] O. E. Kalinovskaya and J. K. Vij, *J. Chem. Phys.* **111**, 10979 (1999).

757 [38] H. Xu, J. K. Vij, A. Rappaport, and N. A. Clark, *Phys. Rev. Lett.* **79**, 249 (1997).

758 [39] U. Manna, J. -K. Song, Yu. P. Panarin, A. Fukuda, and J. K. Vij, *Phys. Rev. E* **77**,
759 04170 (2008).

760 [40] S. P. Sreenilayam, D. M. Agra-Kooijman, V. P. Panov, V. Swaminathan, J. K. Vij, Yu.
761 P. Panarin, A. Kocot, A. Panov, D. Rodriguez-Lojo, P. J. Stevenson, M. R. Fisch, and S.
762 Kumar, *Phys. Rev. E* **95**, 032701 (2017).

763 [41] N. Yadav, V. P. Panov, V. Swaminathan, S. P. Sreenilayam, J. K. Vij, T. S. Perova, R.
764 Dhar, A. Panov, D. Rodriguez-Lojo, and P. J. Stevenson, *Phys. Rev. E* **95**, 062704 (2017).

765 [42] J. Q. Huang, W. D. Meng, and F. L. Qing *J. Fluor. Chem.* **128**, 1469 (2007).